






Band structures in orientation-controlled CuI thin films under epitaxial strainMasao Nakamura ^{1,*}, Sotaro Inagaki,² Yoshihiro Okamura,² Makiko Ogino,² Youtarou Takahashi ^{1,2}, Kiyohiro Adachi ¹,
Daisuke Hashizume ¹, Yoshinori Tokura ^{1,2,3} and Masashi Kawasaki^{1,2}¹RIKEN Center for Emergent Matter Science (CEMS), Wako 351-0198, Japan²Department of Applied Physics and Quantum-Phase Electronics Center (QPEC), University of Tokyo, Bunkyo-ku, Tokyo 113-8656, Japan³Tokyo College, University of Tokyo, Bunkyo-ku, Tokyo 113-8656, Japan

(Received 23 June 2022; accepted 23 August 2022; published 19 September 2022)

Cuprous iodide (CuI) is a wide bandgap (~ 3.1 eV) semiconductor of great recent interest because of its high transparency, high hole conductivity, large exciton binding energy, and sizable spin-orbit interaction. However, studies on single-crystalline thin films have been scarcely reported. Here, we report on the epitaxial growth of single-crystalline CuI films and their optical characterization to elucidate the modification of band structure caused by the anisotropic strain. Thin films were grown by molecular beam epitaxy on nearly lattice-matched (only 0.1%-mismatched) InAs substrates with (001), (110), and (111) crystal orientation, yielding pseudomorphic structures with high lattice coherence and atomic-level flatness. Both reflectance and photoluminescence spectra exhibit sharp exciton profiles over a wide temperature range. We assign the exciton transition energies to deduce the band structure modifications associated with the epitaxial strain varying with temperature and growth orientation. Furthermore, we determine the deformation potentials which relate the strain to the band structure modification. The systematic studies of the strain effect for CuI thin films on various substrate planes will pave the way for the future optoelectronic application of CuI-based heterostructures.

DOI: [10.1103/PhysRevB.106.125307](https://doi.org/10.1103/PhysRevB.106.125307)**I. INTRODUCTION**

The successful development of metal halide perovskite solar cells has accelerated studies on the growth of halide thin films and their physical properties [1–4]. The improvement of the film quality has been crucial for the dramatic enhancement of photovoltaic conversion efficiency [5,6]. Thin films of van der Waals layered metal halides have also attracted recent interest as platforms for unique emergent phenomena such as two-dimensional magnetism and exciton physics [7–12]. To further enhance the device performance as well as to explore quantum phenomena in halide heterostructures with engineered interfaces, single-crystalline thin films with atomic-level flatness are required. One of the ways to realize such high-quality thin films is the heteroepitaxial growth on lattice-matched substrates, as already established in the III–V semiconductors. However, little study has been done on the heteroepitaxy and accompanying epitaxial strain effect in halide thin films.

In this paper, we focus on the heteroepitaxial thin films of cuprous iodide (CuI). CuI is one of the most well-known halide semiconductors with a zinc-blende structure <643 K [13], as depicted in Fig. 1(a). The electronic energy-band

structure of CuI is schematically shown in Fig. 1(b). CuI has a direct bandgap of 3.1 eV [15,16]. Like many zinc-blende semiconductors, the top of the valence band consists of two $J = \frac{3}{2}$ bands (J is the total angular momentum quantum number), called light-hole (LH) and heavy-hole (HH) bands, and is degenerated at the Γ point. The spin-orbit splitting between the $J = \frac{1}{2}$ and $\frac{3}{2}$ bands (Δ_{SO}) is 0.64 eV [17]. This value is considerably larger than that in GaAs (0.34 eV) [18], indicating an even larger spin-orbit interaction in CuI.

Among various physical properties, exciton states have been most intensively studied in CuI and other related cuprous halides (CuBr and CuCl) [16]. Here, excitons have large binding energies (62 meV in CuI), which facilitate the formation of a high-density exciton state and the realization of various exciton complexes like exciton molecules [16,19]. Cuprous halides also have strong exciton-photon coupling, as manifested by the pronounced exciton oscillator strength, potentially enabling the exciton-polariton condensation in microcavity structures [20–22]. In addition, CuI has recently attracted attention as a transparent p -type semiconductor. Hole mobility of $44 \text{ cm}^2 \text{ V}^{-1} \text{ cm}^{-1}$ reported for a single-crystalline bulk sample is one of the highest records among wide bandgap semiconductors, which is promising for hole transport layers in photovoltaic and light-emitting devices as well as for transparent thin-film transistors [23–27].

So far, thin films of CuI have been grown employing a solution process [28–31], vapor or solid-phase iodination [15,32,33], sputtering [24,34–36], pulsed laser deposition [37], and thermal evaporation [15,38,39]. However, these films have polycrystalline or multidomain structures,

*masao.nakamura@riken.jp

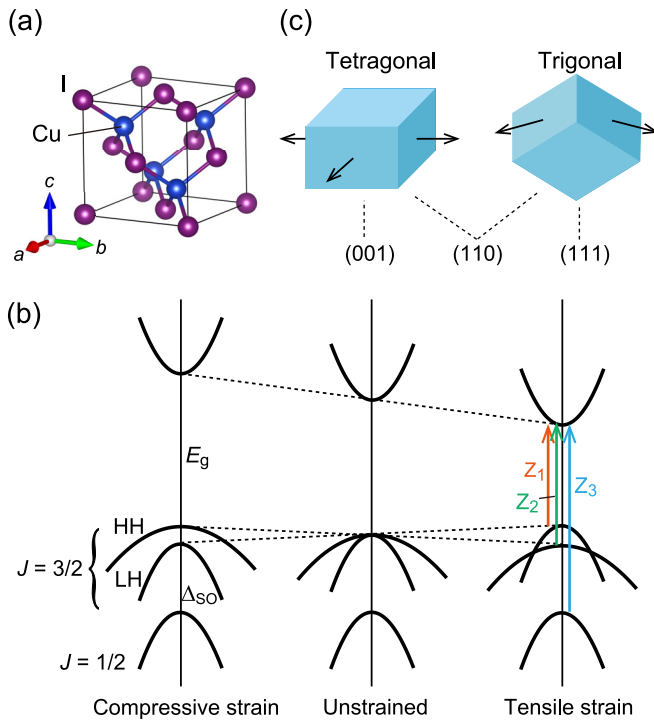


FIG. 1. (a) Crystal structure of cuprous iodide (CuI), drawn with VESTA [14]. (b) Schematic energy band structure of CuI and its modification under biaxial epitaxial strain. The bandgap (E_g) is ~ 3.1 eV, and the spin-orbit splitting Δ_{SO} between the $J = \frac{3}{2}$ and $\frac{1}{2}$ bands is ~ 0.64 eV. HH and LH stand for the heavy-hole and light-hole bands, respectively. Z_1 , Z_2 , and Z_3 represent excitonic transitions from LH, HH, and spin split-off bands to the conduction band, respectively. (c) Schematic illustration of lattice deformations induced by the epitaxial strain from different substrate planes. The present CuI films grown on InAs substrates are subject to a tensile strain of 0.1% at room temperature.

resulting in high-density defects and rough surface morphology. Recently, we have demonstrated that CuI films grown by molecular beam epitaxy (MBE) have much higher crystallinity [40,41]. The films grown on InAs (111) substrates have atomically flat single-crystalline structures without any domain structure [41]. Due to the excellent lattice matching between CuI and InAs (the lattice mismatch is only 0.1% at room temperature), the films experience coherent epitaxial strain, leading to the exceptionally high crystallinity.

In our previous studies, we examined CuI thin film growth only on a (111) substrate plane. Accordingly, the film growth also occurs along the (111) crystal orientation. It should be noted that many other papers have also reported CuI films with preferential (111) crystal orientation except for only one example of (110)-oriented CuI grown on Cu substrate [42], which is presumably because the (111) surface is thermodynamically most stable for CuI. However, control over the crystallographic film orientation is quite important for controlling the electronic states of the films. In fact, the epitaxial strain type depends on its crystallographic orientation. For instance, films grown on a (111) plane experience trigonal deformation, while films grown on a (001) plane are tetragonal,

as depicted in Fig. 1(c). Thus, the strain reduces the crystalline symmetry, which respectively depends on the substrate orientation. The lowered symmetry leads to the band structure modification, as shown in Fig. 1(b), which in turn affects both the transport and optical properties significantly, particularly in strained-layer quantum wells [43,44]. Moreover, the growth orientation affects the spin state in heterostructures. CuI is expected to have enhanced Dresselhaus-type spin splitting due to the large spin-orbit interaction, where the spin-momentum locking pattern is highly dependent on the growth orientation in quantum-well structures [45,46].

In this paper, we demonstrate control of the growth orientation of CuI films by employing the (111), (110), and (001) planes of InAs substrates. All films have pseudomorphic structures with excellent lattice coherency. Reflecting the high crystallinity, the films exhibit sharp exciton spectra. The temperature and growth orientation dependences of the excitonic transitions are systematically investigated to evaluate the modification of the electronic band structure associated with the pseudomorphic strain. The control of the crystalline orientation and band structure via the epitaxial strain will open a route to bring out enhanced optoelectronic functionalities in CuI-based heterostructures.

II. EXPERIMENTAL METHODS

CuI films were grown on (111), (110), and (001) planes of InAs substrate by MBE under similar conditions reported in our previous papers [40,41]. We used commercially available epi-ready substrates without any chemical pretreatment. During the film growth, the flux of CuI was provided by the sublimation of high-purity CuI powder (nominal purity of 5 N) from a Knudsen cell. The cell was heated to $\sim 300^\circ\text{C}$ to yield a beam equivalent pressure of 2×10^{-4} Pa. We first annealed the substrate at 300°C in an MBE chamber to remove the surface contamination. Then we deposited 2-nm-thick CuI film at 160°C as a buffer layer and subsequently carried out the main growth of CuI film at a slightly higher temperature of 180°C . The total thickness of the films is ~ 150 nm.

Crystalline structures and the temperature-dependent lattice constants of the fabricated films were characterized by x-ray diffraction (XRD). We carried out detailed structural analyses at room temperature with a high-resolution four-circle x-ray diffractometer (Rigaku SmartLab). Low-temperature XRD measurements were performed employing a two-circle diffractometer equipped with a cryostat to evaluate the temperature variation of the lattice constants. The surface morphology of the films was determined by atomic force microscopy (AFM).

Reflectance spectra of the thin films were measured with a double-beam spectrophotometer (JASCO MSV-300). The energy resolution of the spectra was ~ 2 meV around the band edge of CuI. We used an Al mirror as a reference. Photoluminescence (PL) spectra were acquired with a 50-cm single monochromator equipped with a charge-coupled device detector. The excitation light was a 325-nm line of a He-Cd laser. The resolution of the PL spectra is ~ 1.7 meV.

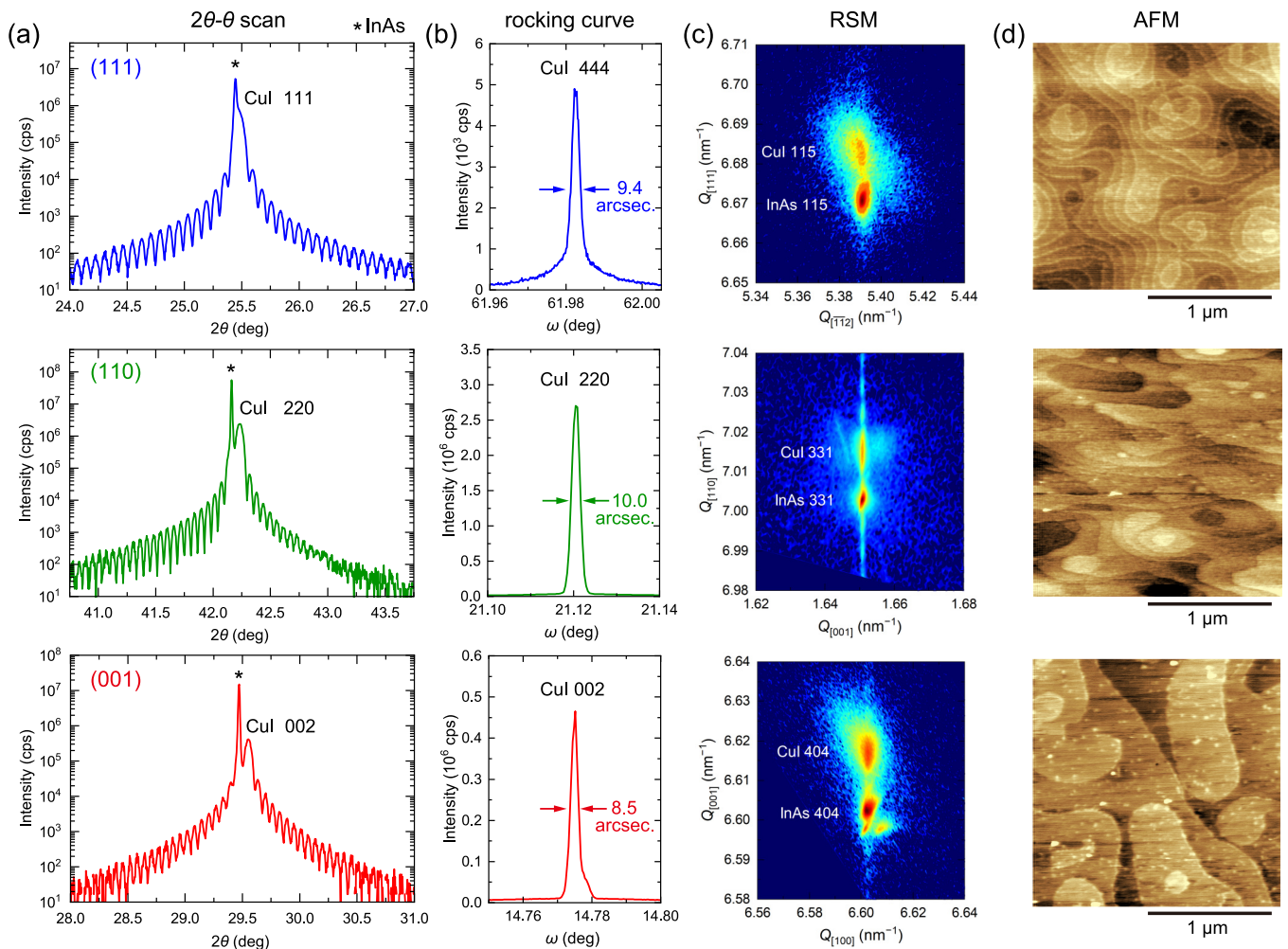


FIG. 2. X-ray diffraction (XRD) patterns and atomic-force microscopy (AFM) images of CuI films grown on the (111), (110), and (001) planes of InAs substrates in the top, middle, and bottom panels, respectively. (a) XRD 2θ - θ scan profiles around 111, 220, and 002 diffraction peaks. Asterisks denote the peaks from the substrates. (b) XRD ω scan profiles (rocking curves) around 444, 220, and 002 diffraction peaks. The full widths at half maxima (FWHM) of the peaks are indicated. (c) XRD reciprocal space maps (RSMs) around 115, 331, and 404 diffraction peaks. (d) AFM images for the films. The results of XRD and AFM for the (111) film are reproduced from Ref. [41], with the permission of AIP Publishing.

III. EXPERIMENTAL RESULTS

A. Crystalline structure and surface morphology

The results of high-resolution XRD obtained at room temperature are displayed in Figs. 2(a)–2(c), where the top, middle, and bottom panels are results for the CuI films on InAs (111), (110), and (001) substrates, respectively. The XRD 2θ - θ scan profiles shown in Fig. 2(a) indicate that the films are epitaxially grown on all the substrates with the same crystalline orientations. The choice of nearly lattice-matched substrate presumably stabilizes the (001)- and (110)-oriented CuI films that have been scarcely realized on other substrates. Since the lattice constant of CuI (6.052 Å) is slightly smaller than that of InAs (6.058 Å) by 0.1%, the films are under tensile strain with slightly smaller out-of-plane lattice constants. The clear Laue fringes observed in all the films signify the high lattice coherence along the out-of-plane direction. The rocking curves shown in Fig. 2(b) exhibit extremely sharp peaks; the peak widths are as narrow as 10 arcsec or less, implying that the films also have quite high in-plane lattice coherence. The

XRD reciprocal space maps (RSMs) displayed in Fig. 2(c) reveal that all the films have pseudomorphic structures with their in-plane lattices locked to the substrates. The fact that peak broadening or peak splitting is absent in the RSM rules out the strain relaxation along the growth direction. The AFM images are shown in Fig. 2(d), which reveal that the surfaces of the films are atomically flat with step-and-terrace structures. From these structural characterizations, we ensure that the three differently oriented pseudomorphic CuI films have excellently high crystallinity.

B. Temperature variation of lattice constants and epitaxial strain

Next, we evaluate the temperature variation of the lattice deformation in the thin films by low-temperature XRD measurements. We determined the out-of-plane lattice constant of the films (a_{\perp}) from 2θ - θ scan measurements. The measurements can also determine the lattice constant of InAs substrate which we assumed to be equivalent to the in-plane lattice

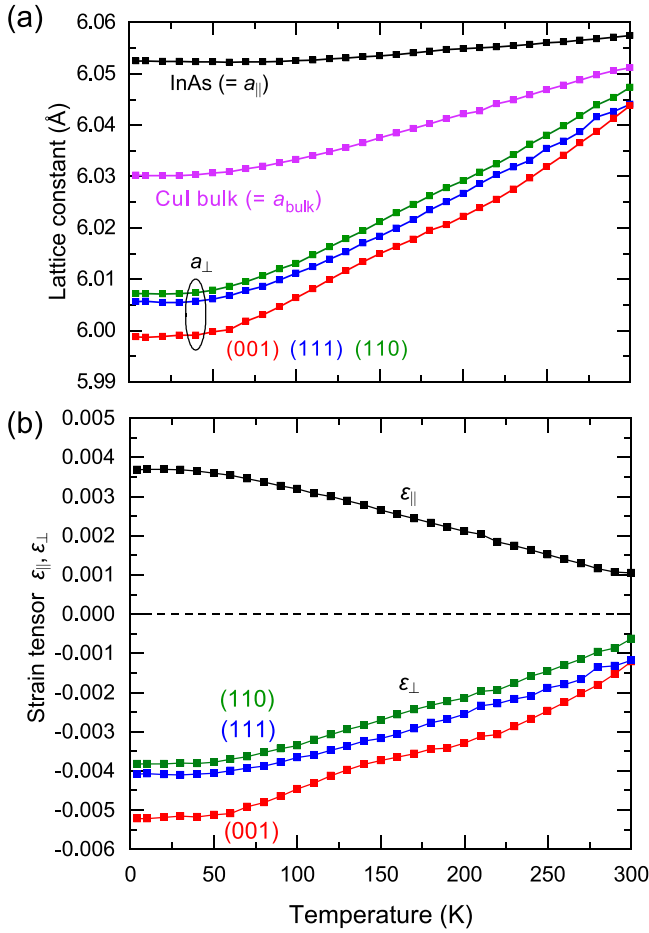


FIG. 3. (a) Temperature dependence of the out-of-plane lattice constants (a_{\perp}) for the CuI films obtained from low-temperature XRD measurements. The values are deduced from the positions of 006, 440, and 333 XRD peaks by transforming them into cubic lattice constants. The red, green, and blue squares represent a_{\perp} for the films on the (001), (110), and (111) substrates, respectively. Also shown is the temperature dependence of the lattice constants for bulk InAs (black squares) and bulk CuI (purple squares), which are measured for InAs substrates and CuI powder. Since all the films have pseudomorphic structures, the in-plane lattice constant of the films ($a_{||}$) is assumed to be equivalent to that of InAs. (b) Temperature dependence of the out-of-plane (ε_{\perp}) and in-plane ($\varepsilon_{||}$) strain tensor components.

constant of the films ($a_{||}$) because of the pseudomorphic structure. We also performed 2θ - θ scans for CuI powder to obtain the lattice constant of unstrained bulk CuI (a_{bulk}).

Figure 3(a) shows the temperature dependence of a_{\perp} , $a_{||}$, and a_{bulk} . It is noticeable that the temperature variation of a_{\perp} is more significant than $a_{||}$ because the linear thermal expansion coefficient for CuI ($\sim 15 \times 10^{-6} \text{ K}^{-1}$ at $\sim 300 \text{ K}$) is much larger than that for InAs ($\sim 4 \times 10^{-6} \text{ K}^{-1}$). Due to the thermal expansion coefficient difference, the tensile strain of the film increases at lower temperatures. We calculated the out-of-plane and in-plane strain tensor components, defined by $\varepsilon_{\perp} = \frac{a_{\perp} - a_{\text{bulk}}}{a_{\text{bulk}}}$ and $\varepsilon_{||} = \frac{a_{||} - a_{\text{bulk}}}{a_{\text{bulk}}}$, respectively. Figure 3(b) depicts their temperature dependence. Theoretically, the relationship between ε_{\perp} and $\varepsilon_{||}$ in pseudomorphic thin films grown on the (001), (110), and (111) substrate planes are

given by

$$\varepsilon_{\perp}^{(001)} = -\frac{2C_{12}}{C_{11}}\varepsilon_{||}, \quad (1)$$

$$\varepsilon_{\perp}^{(110)} = -\frac{C_{11} + C_{12} + 2C_{44}}{C_{11} + 3C_{12} - 2C_{44}}\varepsilon_{||}, \quad (2)$$

$$\varepsilon_{\perp}^{(111)} = -\frac{C_{11} + 2C_{12} + 4C_{44}}{2C_{11} + 4C_{12} - 4C_{44}}\varepsilon_{||}, \quad (3)$$

where C_{11} , C_{12} , and C_{44} are the elastic stiffness constants in cubic crystals [47]. We obtained the relative elastic stiffness constants, C_{12}/C_{11} and C_{44}/C_{11} , by fitting Eqs. (1)–(3) to the experimentally obtained strain tensor values employing the least-squares method (see Supplemental Material [48] for the detailed process of least-squares optimization). The fitting reveals that the relative stiffness constants are almost temperature independent $< 150 \text{ K}$ with $C_{12}/C_{11} = 0.70$ and $C_{44}/C_{11} = 0.36$. These values are very consistent with the previously reported ones, $C_{12}/C_{11} = 0.68$ and $C_{44}/C_{11} = 0.41$, which were obtained in ultrasonic pulse-echo measurements for bulk crystals at room temperature [49]. The strain-induced lattice deformation modifies both the bandgap and band splitting, as depicted in Fig. 1(b). Later, we discuss these band-structure changes based on the values of C_{12}/C_{11} and C_{44}/C_{11} determined in our work.

C. Optical spectra and exciton-polariton characteristics

CuI exhibits clear exciton transitions near the band edge in a wide temperature range due to both the large exciton binding energy and exciton oscillator strength, which is advantageous for sensitively probing the strain-induced modification of the band structure. We measured reflectance spectra of the films to evaluate the resonant energies of the exciton transitions. Figure 4(a) shows the reflectance spectra measured at 20 K. Clear resonant structures are observed at 3.1 and 3.7 eV, which are termed $Z_{1,2}$ and Z_3 transitions, respectively [17]. As depicted in the right-hand panel of Fig. 1(b), $Z_{1,2}$ (Z_3) corresponds to the excitonic resonance associated with the interband transitions between the doubly degenerated valence band top (spin split-off band in the valence band) and the conduction band bottom. The expanded view of the spectra around the $Z_{1,2}$ transitions shown in Fig. 4(b) unveils two resonant structures that indicate the lifting of the degenerate bands at the valence band maximum. As discussed later in more detail, the splitting of the valence band is caused by the tensile epitaxial strain, and the lower-energy peak (higher-energy peak) is related to the transition from the LH (HH) band. Following the definition in Ref. [17], we term the lower-energy peak (higher-energy peak) transition as Z_1 (Z_2) exciton transition, as depicted in Fig. 1(b). Although the spectrum shapes for the three samples are almost identical, the peak positions denoted by the broken lines deviate slightly from each other due to the different symmetry and magnitude of the epitaxial strain.

It is known that the excitons in CuI are strongly coupled to photons to form exciton-polaritons [50,51]. Therefore, the reflectance spectra around the excitonic transitions must be analyzed by including the energy dispersion of the exciton-polariton. Here, we focus only on Z_1 and Z_2 transitions. The

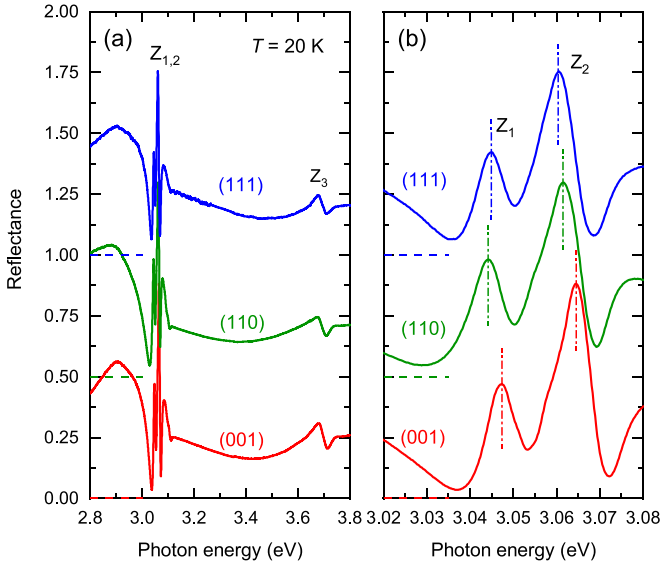


FIG. 4. (a) Reflectance spectra for the CuI films on InAs (111), (110), (001) substrates measured at 20 K. The zero-level baseline (broken lines) is vertically shifted by 0.5 for clarity. The resonant structures at ~ 3.1 and 3.7 eV correspond to the $Z_{1,2}$ and Z_3 excitonic transitions. (b) Expanded view of (a) around the $Z_{1,2}$ transition. Due to the lifting of the degeneracy of light-hole (LH) and heavy-hole (HH) bands, the $Z_{1,2}$ transition splits into the Z_1 and Z_2 transitions. The broken lines are merely guides to the eye to indicate the difference in the resonant energies. The spectrum for the (111) film is reproduced from Ref. [41], with the permission of AIP Publishing.

dielectric function of the exciton-polariton $\varepsilon(\omega, k)$ (ω is a frequency, and k is a wave vector) is given by the following equation [52]:

$$\varepsilon(\omega, k) = \varepsilon_\infty + \sum_{\nu=Z_1, Z_2} \frac{4\pi\alpha_{0\nu}\omega_{\nu T}^2}{\omega_{\nu T}^2 - \omega^2 + \beta_\nu k^2 - i\omega\Gamma_\nu}, \quad (4)$$

where ν labels the Z_1 and Z_2 exciton transitions, $\omega_{\nu T}$ is the transverse exciton resonant frequency, Γ_ν is the broadening factor, ε_∞ is the background dielectric constant, and $\beta_\nu = \hbar\omega_{\nu T}/M_\nu$, where M_ν is the exciton translational mass, and \hbar is the Planck's constant divided by 2π . We set $M_{Z_1} = 0.6 m_0$ and $M_{Z_2} = 2.4 m_0$ (m_0 being the free electron mass) based on the band calculation [53]. Here, $\alpha_{0\nu}$ are given by

$$\alpha_{0Z_1} = \varepsilon_\infty \frac{\omega_{Z_2L}^2 - \omega_{Z_1T}^2}{\omega_{Z_1T}^2} \frac{\omega_{Z_1L}^2 - \omega_{Z_1T}^2}{\omega_{Z_2T}^2 - \omega_{Z_1T}^2}, \quad (5)$$

and

$$\alpha_{0Z_2} = \varepsilon_\infty \frac{\omega_{Z_1L}^2 - \omega_{Z_2T}^2}{\omega_{Z_2T}^2} \frac{\omega_{Z_2L}^2 - \omega_{Z_2T}^2}{\omega_{Z_1T}^2 - \omega_{Z_2T}^2}, \quad (6)$$

where ω_{Z_1L} (ω_{Z_2L}) is the longitudinal exciton frequency of the Z_1 (Z_2) exciton. The dispersion relation of the exciton-polariton is given by the following polarization equation:

$$\varepsilon(\omega, k) = \frac{c^2\omega^2}{k^2}, \quad (7)$$

where c is the velocity of light.

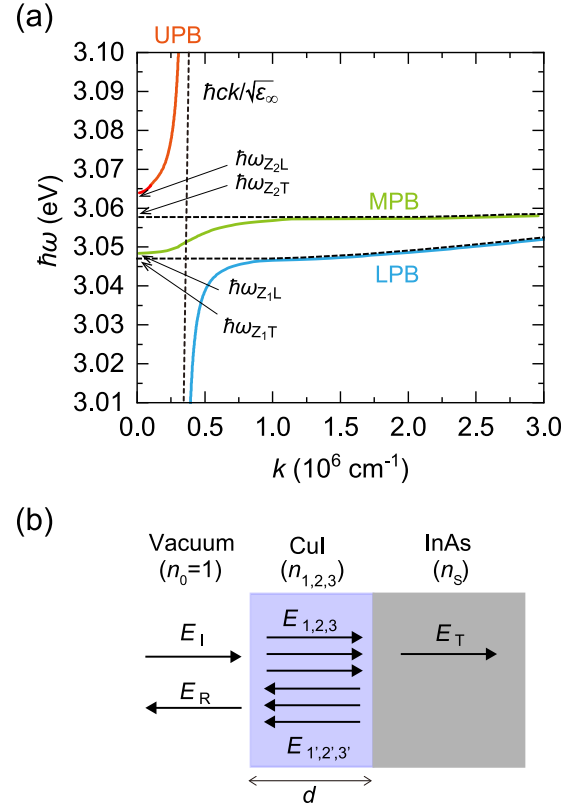


FIG. 5. (a) Exciton-polariton dispersion curves calculated using the parameters shown in Fig. 7. UPB, MBP, and LPB stand for the upper, middle, and lower polariton branches, respectively. The energy levels of transverse exciton $\hbar\omega_{Z_1T}$ ($\hbar\omega_{Z_2T}$) and longitudinal exciton $\hbar\omega_{Z_1L}$ ($\hbar\omega_{Z_2L}$) for the Z_1 (Z_2) exciton are denoted by the arrows. (b) Scheme of layer structure to calculate the reflectance spectra based on the propagation of photon and polariton. E_I , E_R , and E_T represent the electric field of the incident, reflected, and transmitted light, respectively. $E_{1,2,3}$ ($E'_{1,2,3}$) represent the electric field of the three exciton-polariton modes propagating in the film from the surface to the InAs substrate (from the InAs substrate to the surface). n_0 and n_s represent the refractive indices of vacuum and InAs, respectively, and $n_{1,2,3}$ the refractive index for each polariton mode.

The solution of Eqs. (4)–(7) yields three polariton branches, namely, upper, middle, and lower polariton branches, as shown in Fig. 5(a). We calculated the reflectance at each ω by considering the propagation of photons and polaritons in the trilayers consisting of vacuum/CuI film/InAs substrate, as depicted in Fig. 5(b). The model considers the incident and reflected lights (E_I and E_R , respectively) propagating in a vacuum and the transmitted light (E_T) to the substrate. Within the film, light propagates in three polariton modes. We considered three polariton modes propagating from the surface to the bottom of the film ($E_{1,2,3}$) and those propagating in a backward direction after the reflection at the film/substrate interface ($E'_{1,2,3}$). The amplitudes of the electric field of polaritons and photons were determined so that they satisfy the boundary conditions imposed by Maxwell's equation as well as the Pekar-Hopfield-type additional boundary condition, which requires vanishing of the resonant part of

the polarization at the surfaces. These boundary conditions are expressed by the following matrix form [54]:

$$\begin{pmatrix} r \\ f_1 \\ f_2 \\ f_3 \\ f'_1 \\ f'_2 \\ f'_3 \\ t \end{pmatrix} = \begin{pmatrix} -1 & 1 & 1 & 1 & 1 & 1 & 1 & 0 \\ 1 & n_1 & n_2 & n_3 & -n_1 & -n_1 & -n_3 & 0 \\ 0 & e_1 & e_2 & e_3 & e_1^* & e_2^* & e_3^* & -1 \\ 0 & n_1 e_1 & n_2 e_2 & n_3 e_3 & -n_1 e_1^* & -n_2 e_2^* & -n_3 e_3^* & -n_s \\ 0 & \alpha_{Z_1 1} & \alpha_{Z_1 2} & \alpha_{Z_1 3} & \alpha_{Z_1 1} & \alpha_{Z_1 2} & \alpha_{Z_1 3} & 0 \\ 0 & \alpha_{Z_2 1} & \alpha_{Z_2 2} & \alpha_{Z_2 3} & \alpha_{Z_2 1} & \alpha_{Z_2 2} & \alpha_{Z_2 3} & 0 \\ 0 & \alpha_{Z_1 1} e_1 & \alpha_{Z_1 2} e_2 & \alpha_{Z_1 3} e_3 & \alpha_{Z_1 1} e_1^* & \alpha_{Z_1 2} e_2^* & \alpha_{Z_1 3} e_3^* & 0 \\ 0 & \alpha_{Z_2 1} e_1 & \alpha_{Z_2 2} e_2 & \alpha_{Z_2 3} e_3 & \alpha_{Z_2 1} e_1^* & \alpha_{Z_2 2} e_2^* & \alpha_{Z_2 3} e_3^* & 0 \end{pmatrix}^{-1} \begin{pmatrix} 1 \\ 1 \\ 0 \\ 0 \\ 0 \\ 0 \\ 0 \\ 0 \end{pmatrix} \quad (8)$$

Here, $r = \frac{E_R}{E_i}$, $t = \frac{E_T}{E_i}$, $f_j = \frac{E_j}{E_i}$ ($j = 1, 2, 3$), $f'_j = \frac{E'_j}{E_i}$ ($j = 1, 2, 3$), n_s is the refractive index of InAs, n_j is the refractive index of each polariton mode, $e_j = \exp(i \frac{n_j \omega d}{c})$, and $e_j^* = \exp(-i \frac{n_j \omega d}{c})$, where d is the thickness of the film. Also, $\alpha_{Z_1 j}$ and $\alpha_{Z_2 j}$ stand for the excitonic polarizabilities for Z_1 and Z_2 transitions. Furthermore, n_s is fixed to $3.2 + i2.0$ according to the literature value [55].

We fitted the reflectance spectra using the following seven variables characterizing the exciton-polariton state as the fitting parameters: transverse exciton energy ($\hbar\omega_T$), longitudinal-transverse exciton splitting energies (Δ_{L-T}), and Γ for the Z_1 and Z_2 excitons, respectively, plus ε_∞ . The black lines in Fig. 6(a) represent the fitted spectra, which reproduce well the overall features of the experimentally obtained spectra shown by the colored lines. The spectra exhibit oscillatory structure above the Z_1 transition energy, which is attributed to the polariton interference [56]. The obtained values of the fitting parameters are shown in Fig. 7. These parameters vary slightly with the crystallographic film orientation, which will be discussed in Sec. IV. For comparison, the parameters for bulk samples reported in Refs. [51,57] are also given on the rightmost panels of Fig. 7.

Since the Z_1 and Z_2 exciton transitions degenerate without strain, the previously reported exciton-polariton parameters for bulk samples are dominated by the Z_2 exciton having a larger oscillator strength. Consequently, the parameters for the Z_1 exciton have been scarcely elucidated in experiments. We now check for the validity of the parameters for Z_1 exciton obtained in our work by evaluating the ratio of the exciton reduced mass for the Z_1 and Z_2 excitons from their oscillator strengths and comparing it with the results of theoretical band structure calculations. The dielectric function of exciton-polariton described in Eq. (4) indicates that the exciton oscillator strength (f) is proportional to $\alpha_0 \omega_T^2$, where α_0 is defined in Eqs. (5) and (6). Using the parameters shown in Fig. 7, the ratio of the oscillator strength between the Z_1 and Z_2 excitons is 1:3.9. Since the oscillator strength is proportional to the cube of reduced mass ($f \propto \mu^3$) [58], the ratio of μ between the Z_1 and Z_2 excitons is estimated to be 1:1.6. This is very close to the theoretical prediction of 1:1.7 ($\mu_{Z_1} = 0.15m_0$ and $\mu_{Z_2} = 0.26m_0$) [53]. In addition, the experimentally determined exciton reduced mass in bulk samples is $0.27m_0$, which is consistent with the value for the Z_2 exciton derived from the band structure calculations [16]. Therefore, the exciton-polariton parameters derived in this paper are consistent with the results of the band calculation.

We performed similar analyses for the reflectance spectra taken at various temperatures (see Supplemental Material [48]). The experimental spectra can be fitted well in a wide temperature range. The exciton-polariton parameters obtained from the fitting indicate that Δ_{L-T} and ε_∞ are almost constant, while $\hbar\omega_T$ and Γ show significant temperature dependence, as expected. We reported slightly different exciton-polariton parameters in our previous reports on CuI/InAs(111) films [41]. Judging from the consistency between the fitting results

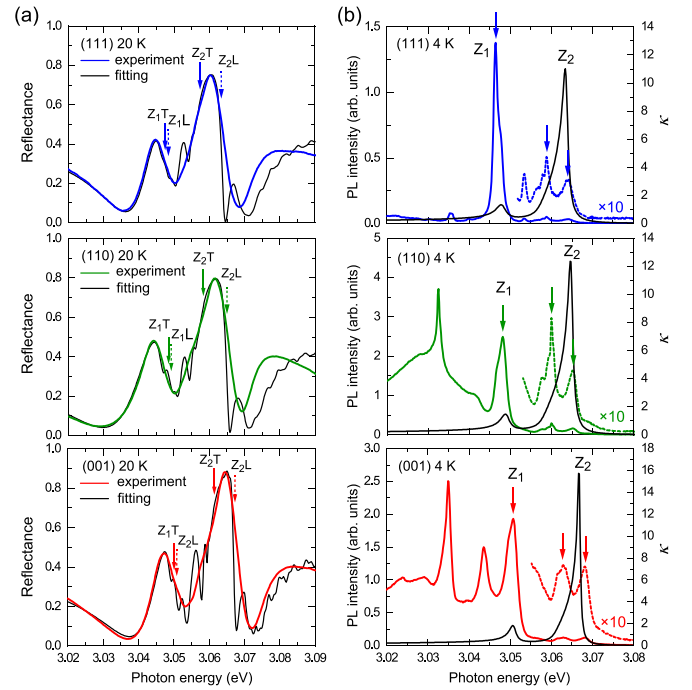


FIG. 6. (a) Colored lines are experimentally obtained reflectance spectra at 20 K. Black lines represent the fitting results. The positions of transverse (Z_{1T} and Z_{2T}) and longitudinal (Z_{1L} and Z_{2L}) exciton energies for the Z_1 and Z_2 excitons are denoted by arrows. (b) Colored lines are photoluminescence (PL) spectra taken at 4 K (left vertical axis). Black lines are the spectra of extinction coefficient (κ) calculated from the dielectric function of the exciton-polariton using the parameters shown in Fig. 7 (right vertical axis). The arrows indicate the peaks in PL spectra associated with the free-exciton emission. In both (a) and (b), the top, middle, and bottom panels are the data for the CuI films on InAs (111), (110), and (001) substrates, respectively. The PL spectrum for the (111) films is reproduced from Ref. [41], with the permission of AIP Publishing.

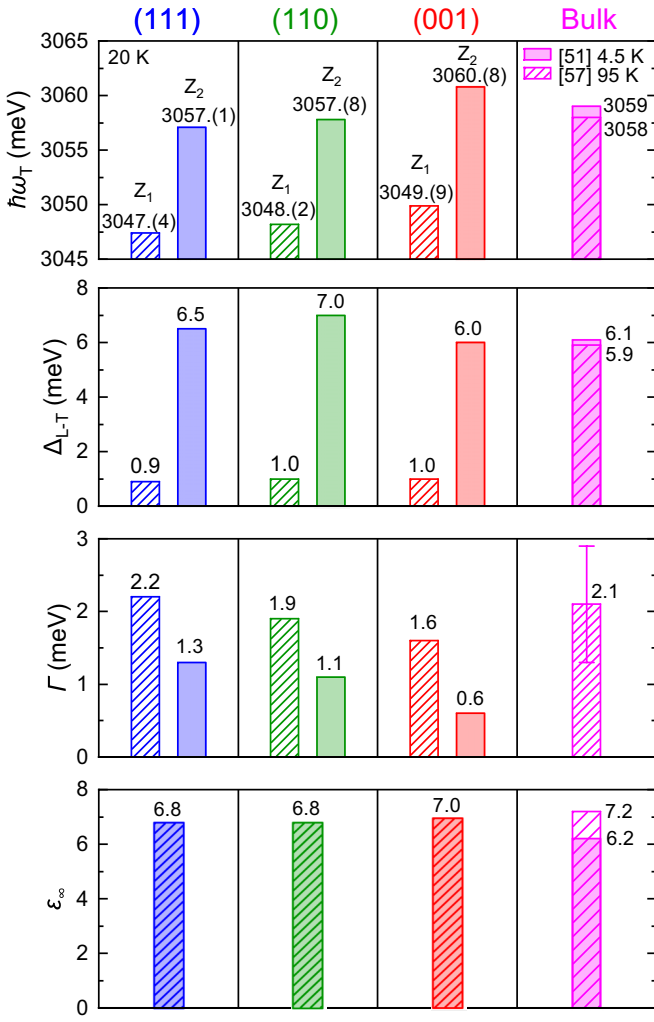


FIG. 7. Characteristic exciton-polariton parameters in the three films determined from the analyses of reflectance spectra measured at 20 K. $\hbar\omega_T$, Δ_{L-T} , Γ , and ϵ_∞ represent the transverse exciton energy, longitudinal-transverse exciton splitting energy, broadening factor, and background dielectric constant, respectively. The hatched and filled bars indicate the parameters for the Z_1 and Z_2 excitons. Data for the films on the (111), (110), and (001) substrates are shown from the leftmost to the right. For comparison, the reported parameters for bulk samples determined from the analyses of reflectance spectra taken at 4.5 K [51] and 95 K [57] are also shown on the rightmost panels by hatched and filled bars, respectively.

for different film orientations and temperatures, we consider that the present results are physically more reasonable.

We calculated the extinction coefficient (κ) by putting the parameters shown in Fig. 7 into Eq. (4) to derive the resonant energies of the excitonic transitions, which are shown by black lines in Fig. 6(b). Colored lines in Fig. 6(b) display the experimentally obtained PL spectra. The spectra of κ have two peaks at ~ 3.05 and 3.065 eV corresponding to the Z_1 and Z_2 excitons, respectively. Since the peaks in PL spectra coincide well with κ peaks, the peaks can be assigned to the free-exciton emission. It is very noticeable that the free-exciton emission associated with the Z_1 transition is very sharp; the full width at half maximum of the luminescence peak is

< 2 meV. Such a clear free-exciton emission has never been observed even in high-quality bulk single crystals of CuI, in which the near band-edge PL spectra at low temperatures are dominated by the luminescence from bound excitons related to the defect/impurity levels [19,50,59,60].

The Z_2 exciton luminescence indicates a splitting into two peaks in Fig. 6(b). We assign that this doublet structure comes from the exciton-polariton luminescence [61]. This assignment is supported by the fact that the splitting energy of ~ 6 meV is very close to the value of Δ_{L-T} for the Z_2 exciton shown in Fig. 7. The peak splitting in the Z_1 exciton luminescence is less obvious, partly because of the insufficient resolution of the PL measurement system to deconvolute the two polariton emissions. However, the presence of overlapped two peaks is discernible in all three films by close looking. More explicit peak splitting is observed at a slightly elevated temperature for the film on the (111) substrate [see the PL spectra at 30 K in Fig. 8(a)], where the peak splitting is ~ 1 meV, also consistent with Δ_{L-T} for the Z_1 exciton shown in Fig. 7. These results indicate that a well-defined exciton-polariton state is formed in our films, which reinforces the validity of analyzing the reflection spectra in the exciton-polariton framework.

The PL spectra also have several strong luminescence lines other than the free-exciton luminescence, particularly in the films on the (110) and (001) substrates. These luminescence lines can be interpreted as the emission of the bound excitons associated with some defects caused by the laser irradiation because their intensities increased during the PL measurements.

Figure 8 displays the temperature dependence of the PL spectra. The Z_1 and Z_2 exciton resonance energies derived from the analyses of the reflectance spectra are denoted by triangles. In the PL spectra, two peaks are prominent in the intermediate temperature range (100–200 K). Their position coincides well with the Z_1 and Z_2 exciton energies indicated by triangles, which is clear evidence that the PL lines originate from the free-exciton luminescence. In the high-temperature range, the two PL peaks merge into one due to the reduced splitting between the Z_1 and Z_2 transitions and the thermal broadening of the peak widths.

IV. DISCUSSION ON THE STRAIN-INDUCED BAND STRUCTURE MODIFICATION

As revealed by XRD measurements, the CuI films on InAs substrates are under coherent tensile strain, and the strain is more pronounced with decreasing temperature due to the thermal expansion mismatch between the substrate and the film. The tensile strain results in the lifting of the degenerate LH and HH bands as well as the reduction of the bandgap, as depicted in the inset of Fig. 9(a). The effective strain Hamiltonian for $J = \frac{3}{2}$ valence bands in zinc-blende semiconductors is given as follows [63,64]:

$$\mathcal{H} = a(\epsilon_{xx} + \epsilon_{yy} + \epsilon_{zz}) + b \left[\left(J_x^2 - \frac{J^2}{3} \right) \epsilon_{xx} + \text{c.p.} \right] + \frac{d}{\sqrt{3}} [(J_x J_y + J_y J_x) \epsilon_{xy} + \text{c.p.}], \quad (9)$$

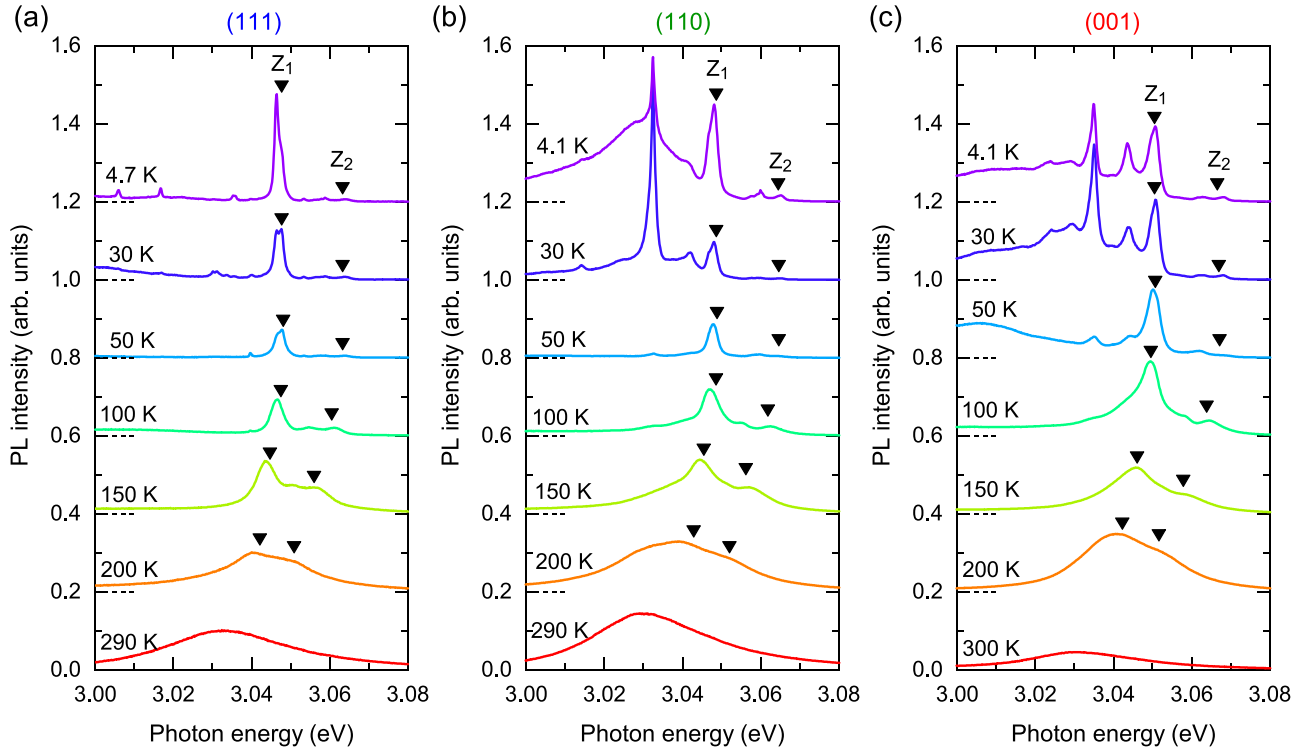


FIG. 8. Temperature dependence of photoluminescence (PL) spectra. (a)–(c) Spectra for the films on the (111), (110), and (001) substrates, respectively. The zero-level baseline (broken lines) for the spectrum is vertically shifted by 0.2 for clarity. The Z_1 and Z_2 exciton transition energies are denoted by triangles which are determined from the analyses of the reflectance spectra.

where a , b , and d are three deformation potentials associated with hydrostatic, tetragonal, and trigonal deformations, respectively, ε_{ij} is the strain tensor, J_i is the total angular momentum operator, and c.p. stands for cyclic permutation. The first term in Eq. (9) induces the bandgap change, while the second and third terms bring about the splitting of the degenerate valence bands. Hereafter, we evaluate the strain-induced band structure modification and deformation potentials based on the transition energies of the Z_1 and Z_2 excitons. Note that the two excitons should have different binding energies due to their different reduced masses, which requires additional but small corrections in the evaluation of the band structures. In the following discussions, we assume that this correction is negligible when the strain is large enough, like previous works [65,66].

We first consider the bandgap change (ΔE_g) induced by the hydrostatic deformation, i.e., the difference in the bandgap between the film (strained state) and bulk (unstrained state). Here, ΔE_g is nearly equivalent to the difference between the average of the Z_1 and Z_2 transverse exciton energies in the films, namely, $(\hbar\omega_{Z_1T} + \hbar\omega_{Z_2T})/2$, and the $Z_{1,2}$ transverse exciton energy in bulk ($\hbar\omega_{Z_{1,2}T}$). The temperature dependence of $(\hbar\omega_{Z_1T} + \hbar\omega_{Z_2T})/2$ in the three films is shown in Fig. 9(a). We also plot the temperature dependence of $\hbar\omega_{Z_{1,2}T}$ determined from two-photon absorption measurements for bulk CuI [62]. The small temperature dependence of $\hbar\omega_{Z_{1,2}T}$ above 150 K is due to the overlapping of the longitudinal and transverse excitons associated with the thermal broadening, as mentioned in Ref. [62]. The figure indicates that ΔE_g is negative in all three films, and its absolute magnitude increases in the order of (001), (110), and (111) orientation.

In Fig. 10(a) is shown ΔE_g derived from the difference in the exciton transition energies between the bulk and films as a function of in-plane strain (ε_{\parallel}). Here, ΔE_g is roughly proportional to ε_{\parallel} , and the slope is related to the deformation potential a . The theoretical expressions for ΔE_g in pseudomorphic thin films grown on the three substrate planes derived from Eq. (9) are given as follows:

$$\Delta E_g^{(001)} = 2a \frac{C_{11} - C_{12}}{C_{11}} \varepsilon_{\parallel} = 0.60a\varepsilon_{\parallel}, \quad (10)$$

$$\Delta E_g^{(110)} = 2a \frac{C_{11} - C_{12} + 6C_{44}}{C_{11} + C_{12} + 2C_{44}} \varepsilon_{\parallel} = 1.02a\varepsilon_{\parallel}, \quad (11)$$

$$\Delta E_g^{(111)} = 2a \frac{4C_{44}}{C_{11} + C_{12} + 4C_{44}} \varepsilon_{\parallel} = 1.13a\varepsilon_{\parallel}, \quad (12)$$

where we used temperature-dependent ε_{\parallel} shown in Fig. 3(b) and fixed values of $C_{12}/C_{11} = 0.70$ and $C_{44}/C_{11} = 0.36$ determined from the low-temperature XRD measurements. We derived $a = -1.1$ eV as the best least-squares fit of Eqs. (10)–(12) to the experimental results.

Next, we discuss the energy splitting between the LH and HH bands at the Γ point resulting from the tetragonal and trigonal deformations ($\Delta E_{\text{HH-LH}}$). Here, we define that the sign of $\Delta E_{\text{HH-LH}}$ is negative when the HH band locates at a lower energy than the LH band. Also, $\Delta E_{\text{HH-LH}}$ is nearly equivalent to the difference between the Z_1 and Z_2 transverse exciton energies, namely, $\hbar\omega_{Z_1T} - \hbar\omega_{Z_2T}$. We show in Fig. 9(c) the temperature dependence of $\hbar\omega_{Z_1T} - \hbar\omega_{Z_2T}$ for the three films.

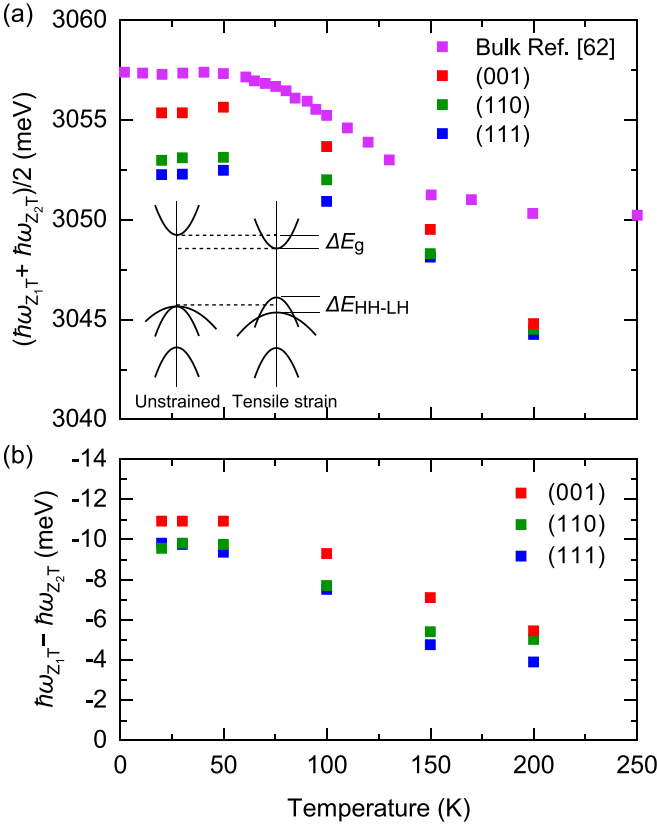


FIG. 9. (a) Temperature dependence of the average of the Z_1 and Z_2 transverse exciton energies $(\hbar\omega_{Z_1T} + \hbar\omega_{Z_2T})/2$ in the CuI films. The purple squares show the temperature dependence of the $Z_{1,2}$ transverse exciton energy for unstrained CuI ($\hbar\omega_{Z_{1,2}T}$) determined from two-photon absorption measurements for a bulk sample reported in Ref. [62]. The energy difference between them corresponds nearly to the bandgap change induced by the strain (ΔE_g). The inset shows the schematic band structures for unstrained and tensile-strained case. It also shows the definition of the ΔE_g and the splitting between the heavy-hole (HH) and light-hole (LH) bands (ΔE_{HH-LH}). (b) Temperature dependence of $\hbar\omega_{Z_1T} - \hbar\omega_{Z_2T}$ is nearly equivalent to ΔE_{HH-LH} . In both panels, the red, green, and blue squares indicate the results for the film on (001), (110), and (111) substrates, respectively.

The theoretical expressions for ΔE_{HH-LH} in pseudomorphic thin films derived from Eq. (9) are given as follows:

$$\Delta E_{HH-LH}^{(001)} = 2b \frac{C_{11} + 2C_{12}}{C_{11}} \varepsilon_{\parallel} = 4.80b\varepsilon_{\parallel}, \quad (13)$$

$$\begin{aligned} \Delta E_{HH-LH}^{(110)} &= -2\sqrt{b^2 + d^2} \frac{C_{11} + 2C_{12}}{C_{11} + C_{12} + 2C_{44}} \varepsilon_{\parallel} \\ &= -1.98\sqrt{b^2 + d^2} \varepsilon_{\parallel}, \end{aligned} \quad (14)$$

$$\Delta E_{HH-LH}^{(111)} = 2\sqrt{3}d \frac{C_{11} + 2C_{12}}{C_{11} + 2C_{12} + 4C_{44}} \varepsilon_{\parallel} = 2.17d\varepsilon_{\parallel}, \quad (15)$$

where we again used the experimentally determined temperature dependence of ε_{\parallel} and fixed values of $C_{12}/C_{11} = 0.70$ and $C_{44}/C_{11} = 0.36$. Equations (13)–(15) imply that ΔE_{HH-LH} in the films on the (001) and (111) substrates are affected only by the second and third terms of Eq. (9), respectively, as can be

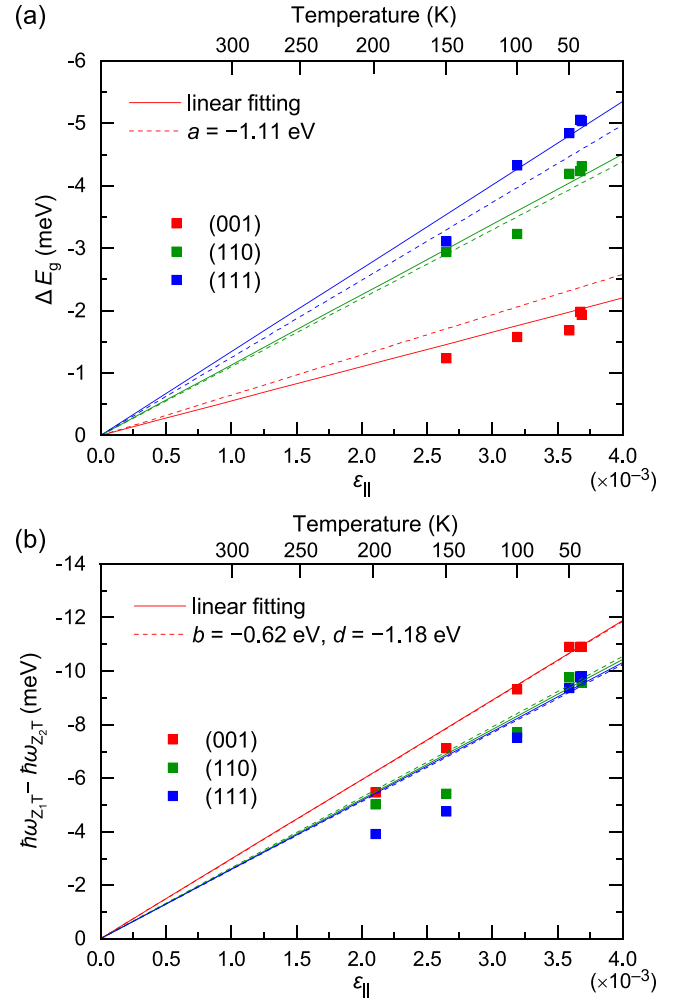


FIG. 10. (a) Variation of ΔE_g as a function of ε_{\parallel} . The solid lines are the fitting results assuming a linear relationship between ΔE_g and ε_{\parallel} . The dashed lines are the calculation results for $a = -1.11$ eV in Eqs. (10)–(12). (b) Variation of $\hbar\omega_{Z_1T} - \hbar\omega_{Z_2T}$ as a function of ε_{\parallel} . The solid lines are the fitting results assuming a linear relationship between $\hbar\omega_{Z_1T} - \hbar\omega_{Z_2T}$ and ε_{\parallel} . The dashed lines are the results of the calculation for $b = -0.62$ eV and $d = -1.18$ eV in Eqs. (13)–(15). In both panels, temperature is shown on the upper axis to indicate the correspondence between temperature and ε_{\parallel} .

intuitively understood from the deformation modes depicted in Fig. 1(c). Both terms have an equal contribution in the film on the (110) substrate.

Figure 10(b) shows the variation of $\hbar\omega_{Z_1T} - \hbar\omega_{Z_2T}$ as a function of ε_{\parallel} . It indicates that the exciton splitting energy varies almost linearly with ε_{\parallel} for large ε_{\parallel} but deviates from the linear dependence at small ε_{\parallel} . We obtained $b = -0.6$ eV and $d = -1.2$ eV from the least-squares fitting of experimental results with Eqs. (13)–(15) in the range of large ε_{\parallel} . The discrepancy between $\hbar\omega_{Z_1T} - \hbar\omega_{Z_2T}$ and ΔE_{HH-LH} caused by the difference in the binding energies for the two excitons will be more crucial when the splitting energy is small, which is one possible reason for the deviation from the linear dependence at small ε_{\parallel} .

Sauder *et al.* [66] have reported the deformation potential values of $a = -0.99$ eV, $b = -0.65$ eV, and $d = -1.67$ eV,

which are determined from reflectance spectra at 1.5 K for bulk single crystals under uniaxial stress along [001] and [111] axes. In another paper, Blacha *et al.* [65] have reported $a = -1.1$ eV and $d = -1.4$ eV as determined from the absorption spectra at 100 K for a thermally deposited (111)-oriented polycrystalline film under uniaxial stress. The presently obtained values ($a = -1.1$ eV, $b = -0.6$ eV, and $d = -1.2$ eV) are in reasonably good agreement with those in previous reports. Although we have not ascertained the reasons for the slight discrepancy, we consider that the difference in the strain type (uniaxial or biaxial) and in the crystalline quality may affect it. Bulk crystals of CuI are known to exhibit structural phase transitions at a relatively low hydrostatic pressure of ~ 1 GPa [13]. Bulk samples or strain-free films employed in the previous measurements can undergo similar phase transitions under uniaxial pressure, which hamper the accurate estimation of the deformation potentials. On the other hand, such phase transitions are unlikely to occur in the present case because the zinc-blende structure of the films is further stabilized by the pseudomorphic epitaxial strain from the zinc-blende-type InAs substrates. We also emphasize that the crystallinity of our films is much higher than that of the most bulk single crystals, judging from the results of XRD and PL spectra. Exciton transition energies are determined with much higher accuracy in the present case owing to the significantly sharp resonant structure. The strain tensor and the deformation potentials are determined so that they can consistently reproduce the experimentally obtained band structure modification in the films of three different strain orientations as well as its temperature dependence. Thus, we expect that the present evaluation has even more improved reliability.

Let us briefly discuss the materials dependence. The obtained deformation potential values are much smaller than those in the III-V semiconductors, for instance, $a = -8.3$ eV, $b = -2.0$ eV, and $d = -4.8$ eV in GaAs [18]. The small deformation potentials imply the ionic nature of the chemical bonds in CuI, leading to a pronounced piezoelectric response [49]. The coupling between the piezoelectricity and the stable exciton state in CuI potentially induces intriguing nonlinear

optical phenomena like the exciton shift current and exciton Hall effect [67–69].

V. CONCLUSIONS

We examined the heteroepitaxial structures and optical properties of strained cuprous iodide (CuI) thin films grown on nearly lattice-matched InAs substrates with (111), (110), and (001) planes by MBE. Fabricated thin films have pseudomorphic structures, indicating that the growth orientation could be controlled via the epitaxial strain. The films have excellent crystallinity manifested by the high lattice coherence and atomic-level surface flatness. The epitaxial strain increases with decreasing temperature due to the difference in the thermal expansion coefficient between CuI and InAs. The influence of the epitaxial strain on the electronic band structure was deduced from the energy of excitonic transition lines. Both reflectance and PL spectra of the films exhibit sharp resonant structures associated with exciton transitions. Upon lowering temperature, these exciton resonance lines shift in energy and develop splitting which indicates the bandgap change and lifting of the band degeneracy, respectively. We precisely determined the exciton resonance energies from the analyses of the reflectance spectra and derived the deformation potentials. The heteroepitaxial thin film growth and detailed assignment of the band structure modification demonstrated in this paper pave the way for studying quantum phenomena emerging in CuI-based quantum wells and heterostructures.

ACKNOWLEDGMENTS

The authors would like to thank T. Arima, N. Nagaosa, and G. Y. Guo for fruitful discussions, and D. Maryenko for critical reading of the manuscript. We also thank M. Watanuki at Advanced Manufacturing Support Team in RIKEN for making the sample holder for low-temperature XRD experiments. This paper was supported by JSPS KAKENHI (22H04958 and 20H02626).

-
- [1] A. Kojima, K. Teshima, Y. Shirai, and T. Miyasaka, *J. Am. Chem. Soc.* **131**, 6050 (2009).
 - [2] M. A. Green, A. Ho-Baillie, and H. J. Snaith, *Nat. Photonics* **8**, 506 (2014).
 - [3] S. D. Stranks and H. J. Snaith, *Nat. Nanotechnol.* **10**, 391 (2015).
 - [4] A. K. Jena, A. Kulkarni, and T. Miyasaka, *Chem. Rev.* **119**, 3036 (2019).
 - [5] W. A. Dunlap-Shohl, Y. Zhou, N. P. Padture, and D. B. Mitzi, *Chem. Rev.* **119**, 3193 (2019).
 - [6] T. Soto-Montero, W. Soltanpoor, and M. Morales-Masis, *APL Mater.* **8**, 110903 (2020).
 - [7] B. Huang, G. Clark, E. Navarro-Moratalla, D. R. Klein, R. Cheng, K. L. Seyler, D. Zhong, E. Schmidgall, M. A. McGuire, D. H. Cobden *et al.*, *Nature (London)* **546**, 270 (2017).
 - [8] W. Chen, Z. Sun, Z. Wang, L. Gu, X. Xu, S. Wu, and C. Gao, *Science* **366**, 983 (2019).
 - [9] Q. Song, C. A. Occhialini, E. Ergecen, B. Ilyas, D. Amoroso, P. Barone, J. Kapeghian, K. Watanabe, T. Taniguchi, A. S. Botana *et al.*, *Nature (London)* **602**, 601 (2022).
 - [10] Y. Hu, Y. Guo, Y. Wang, Z. Chen, X. Sun, J. Feng, T.-M. Lu, E. Wertz, and J. Shi, *J. Mater. Res.* **32**, 3992 (2017).
 - [11] T. Yasunami, M. Nakamura, S. Inagaki, S. Toyoda, N. Ogawa, Y. Tokura, and M. Kawasaki, *Appl. Phys. Lett.* **119**, 243101 (2021).
 - [12] X. Cai, Z. Xu, S.-H. Ji, N. Li, and X. Chen, *Chinese Phys. B* **30**, 028102 (2021).
 - [13] E. Rapoport and C. W. Pistorius, *Phys. Rev.* **172**, 838 (1968).
 - [14] K. Momma and F. Izumi, *J. Appl. Crystallogr.* **44**, 1272 (2011).
 - [15] M. Grundmann, F. L. Schein, M. Lorenz, T. Böntgen, J. Lenzner, and H. von Wenckstern, *Phys. Status Solidi A* **210**, 1671 (2013).
 - [16] M. Ueta, H. Kanzaki, K. Kobayashi, Y. Toyozawa, and E. Hanamura, *Excitonic Processes in Solids* (Springer-Verlag, Berlin, Heidelberg, 1986).

- [17] M. Cardona, *Phys. Rev.* **129**, 69 (1963).
- [18] I. Vurgaftman, J. R. Meyer, and L. R. Ram-Mohan, *J. Appl. Phys.* **89**, 5815 (2001).
- [19] T. Goto, T. Takahashi, and M. Ueta, *J. Phys. Soc. Jpn.* **24**, 314 (1968).
- [20] T. Byrnes, N. Y. Kim, and Y. Yamamoto, *Nat. Phys.* **10**, 803 (2014).
- [21] M. Nakayama, M. Kameda, T. Kawase, and D. Kim, *Phys. Rev. B* **83**, 235325 (2011).
- [22] M. Nakayama, K. Miyazaki, T. Kawase, and D. Kim, *Phys. Rev. B* **83**, 075318 (2011).
- [23] D. Chen, Y. Wang, Z. Lin, J. Huang, X. Z. Chen, D. Pan, and F. Huang, *Cryst. Growth Des.* **10**, 2057 (2010).
- [24] C. Yang, M. Kneiß, M. Lorenz, and M. Grundmann, *Proc. Natl. Acad. Sci. USA* **113**, 12929 (2016).
- [25] A. Liu, H. Zhu, M. G. Kim, J. Kim, and Y. Y. Noh, *Adv. Sci.* **8**, 2100546 (2021).
- [26] J. A. Christians, R. C. Fung, and P. V. Kamat, *J. Am. Chem. Soc.* **136**, 758 (2014).
- [27] G. A. Sepalage, S. Meyer, A. Pascoe, A. D. Scully, F. Huang, U. Bach, Y.-B. Cheng, and L. Spiccia, *Adv. Funct. Mater.* **25**, 5650 (2015).
- [28] S. Inudo, M. Miyake, and T. Hirato, *Phys. Status Solidi A* **210**, 2395 (2013).
- [29] A. Liu, H. Zhu, W. T. Park, S. J. Kim, H. Kim, M. G. Kim, and Y. Y. Noh, *Nat. Commun.* **11**, 4309 (2020).
- [30] S. Lee, H. J. Lee, Y. Ji, S. M. Choi, K. H. Lee, and K. Hong, *J. Mater. Chem. C* **8**, 9608 (2020).
- [31] H. J. Lee, S. Lee, Y. Ji, K. G. Cho, K. S. Choi, C. Jeon, K. H. Lee, and K. Hong, *ACS Appl. Mater. Interfaces* **11**, 40243 (2019).
- [32] N. Yamada, R. Ino, H. Tomura, Y. Kondo, and Y. Ninomiya, *Adv. Electron. Mater.* **3**, 1700298 (2017).
- [33] S. D. Baek, D. K. Kwon, Y. C. Kim, and J. M. Myoung, *ACS Appl. Mater. Interfaces* **12**, 6037 (2020).
- [34] T. Tanaka, K. Kawabata, and M. Hirose, *Thin Solid Films* **281**, 179 (1996).
- [35] C. Yang, D. Souchay, M. Kneiß, M. Bogner, H. M. Wei, M. Lorenz, O. Oeckler, G. Benstetter, Y. Q. Fu, and M. Grundmann, *Nat. Commun.* **8**, 16076 (2017).
- [36] W. Yu, G. Benndorf, Y. Jiang, K. Jiang, C. Yang, M. Lorenz, and M. Grundmann, *Phys. Status Solidi RRL* **15**, 2000431 (2020).
- [37] P. Storm, M. Bar, G. Benndorf, S. Selle, C. Yang, H. von Wenckstern, M. Grundmann, and M. Lorenz, *APL Mater.* **8**, 091115 (2020).
- [38] D. Kim, M. Nakayama, O. Kojima, I. Tanaka, H. Ichida, T. Nakanishi, and H. Nishimura, *Phys. Rev. B* **60**, 13879 (1999).
- [39] K. Tennakone, G. Kumara, I. Kottegoda, V. Perera, G. Aponsu, and K. Wijayantha, *Sol. Energy Mater. Sol. Cells* **55**, 283 (1998).
- [40] S. Inagaki, M. Nakamura, N. Aizawa, L. C. Peng, X. Z. Yu, Y. Tokura, and M. Kawasaki, *Appl. Phys. Lett.* **116**, 192105 (2020).
- [41] S. Inagaki, M. Nakamura, Y. Okamura, M. Ogino, Y. Takahashi, L. C. Peng, X. Z. Yu, Y. Tokura, and M. Kawasaki, *Appl. Phys. Lett.* **118**, 012103 (2021).
- [42] Z. Zheng, A. Liu, S. Wang, B. Huang, K. W. Wong, X. Zhang, S. K. Hark, and W. M. Lau, *J. Mater. Chem.* **18**, 852 (2008).
- [43] G. Osbourn, *J. Appl. Phys.* **53**, 1586 (1982).
- [44] E. P. O'Reilly, *Semicond. Sci. Technol.* **4**, 121 (1989).
- [45] G. Dresselhaus, *Phys. Rev.* **100**, 580 (1955).
- [46] S. D. Ganichev and L. E. Golub, *Phys. Status Solidi B* **251**, 1801 (2014).
- [47] J. M. Hinckley and J. Singh, *Phys. Rev. B* **42**, 3546 (1990).
- [48] See Supplemental Material at <http://link.aps.org/supplemental/10.1103/PhysRevB.106.125307> for the detailed process of least-squares optimization and reflectance spectra at various temperatures.
- [49] R. Hanson, J. Hallberg, and C. Schwab, *Appl. Phys. Lett.* **21**, 490 (1972).
- [50] E. Krüger, M. S. Bar, S. Blaurock, L. Trefflich, R. Hildebrandt, A. Müller, O. Herrfurth, G. Benndorf, H. von Wenckstern, H. Krautscheid *et al.*, *APL Mater.* **9**, 121102 (2021).
- [51] S. Suga, K. Cho, Y. Niji, J. C. Merle, and T. Sauder, *Phys. Rev. B* **22**, 4931 (1980).
- [52] J. J. Hopfield and D. G. Thomas, *Phys. Rev.* **132**, 563 (1963).
- [53] J. Wang, J. Li, and S.-S. Li, *J. Appl. Phys.* **110**, 054907 (2011).
- [54] B. Foy, E. McGlynn, A. Cowley, P. J. McNally, and M. O. Henry, *J. Appl. Phys.* **112**, 033505 (2012).
- [55] D. E. Aspnes and A. A. Studna, *Phys. Rev. B* **27**, 985 (1983).
- [56] T. Mita and N. Nagasawa, *Solid State Commun.* **44**, 1003 (1982).
- [57] M. Certier, M. Soltani, O. Pages, A. Zaoui, W. Sekkal, and H. Aourag, *Mater. Sci. Eng. B* **58**, 234 (1999).
- [58] R. J. Elliott, *Phys. Rev.* **108**, 1384 (1957).
- [59] V. Nikitenko, S. Stoyukhin, V. Popolitov, and Y. M. Mininzon, *J. Appl. Spectrosc.* **34**, 410 (1981).
- [60] M. Wille, E. Krüger, S. Blaurock, V. Zviagin, R. Deichsel, G. Benndorf, L. Trefflich, V. Gottschalch, H. Krautscheid, R. Schmidt-Grund *et al.*, *Appl. Phys. Lett.* **111**, 031105 (2017).
- [61] S. Suga and T. Koda, *Phys. Status Solidi B* **66**, 255 (1974).
- [62] J. Serrano, C. Schweitzer, C. T. Lin, K. Reimann, M. Cardona, and D. Fröhlich, *Phys. Rev. B* **65**, 125110 (2002).
- [63] G. L. Bir and G. E. Pikus, *Symmetry and Strain-Induced Effects in Semiconductors* (Wiley, New York, 1974).
- [64] Y. Y. Peter and M. Cardona, *Fundamentals of Semiconductors: Physics and Materials Properties* (Springer, Heidelberg, 2010).
- [65] A. Blacha, S. Ves, and M. Cardona, *Phys. Rev. B* **27**, 6346 (1983).
- [66] T. Sauder, A. Daunois, J. Deiss, and J. Merle, *Solid State Commun.* **51**, 323 (1984).
- [67] T. Morimoto and N. Nagaosa, *Phys. Rev. B* **94**, 035117 (2016).
- [68] M. Sotome, M. Nakamura, T. Morimoto, Y. Zhang, G. Y. Guo, M. Kawasaki, N. Nagaosa, Y. Tokura, and N. Ogawa, *Phys. Rev. B* **103**, L241111 (2021).
- [69] M. Onga, Y. Zhang, T. Ideue, and Y. Iwasa, *Nat. Mater.* **16**, 1193 (2017).